JOURNAL OF THERMOPHYSICS AND HEAT TRANSFER
Vol. 14, No. 2, April–June 2000

Navier–Stokes Computation of Flows in Arc Heaters

Kyu Hong Kim* and Oh Hyun Rho†
Seoul National University, Seoul 151-742, Republic of Korea
and
Chul Park‡
Thermosciences Institute, Moffett Field, California 94035

The existing computer code ARCFLO, which calculates the flow through the constricted-arc heater, is modified and expanded by the use of the modern computational fluid dynamics technique. The entire flowfield within an arc-heated wind tunnel, that is, from the upstream electrode chamber to the nozzle exit, is described by the Navier–Stokes equations, but the joule heating and radiative transfer phenomena are described as in the ARCFLO code. The modeling of turbulence in the constrictor region is different from that in ARCFLO. The code developed in the present work, tentatively designated as Arcflo2, requires only the mass flow rate and electrical current as inputs and describes the flow conditions from the upstream electrode region to the nozzle throat. The code reproduces the measured operating characteristics of several wind tunnels closer than the ARCFLO code.

Nomenclature

c_p = specific heat at constant pressure, J/(kg · K)
D_c = diameter of constrictor, m
D_t = diameter of nozzle throat, m
E = voltage gradient, V/m
$\boldsymbol{E}$ = inviscid flux vector in streamwise direction
E_ν = black body emission, W · s/(m^2 · sr)
$\boldsymbol{E}_v$ = viscous flux vector in streamwise direction
e_t = total energy, m^2/s^2
$\boldsymbol{F}$ = inviscid flux vector in radial direction
$\boldsymbol{F}_v$ = viscous flux vector in radial direction
G = radiant flux in angular direction
H = total enthalpy, m^2/s^2
$\boldsymbol{H}$ = axisymmetric inviscid source vector
$\boldsymbol{H}_v$ = axisymmetric viscous source vector
h = enthalpy, J/kg
$\bar{h}$ = mass-averaged enthalpy, J/kg
$\bar{h}_\infty$ = asymptotic mass-averaged enthalpy in an infinite constrictor, J/kg
I = current, A
$\boldsymbol{I}$ = joule heating source vector
I_ν = specific radiative intensity, W · s/(m^2 · sr)
j = current density, A/m^2
k = thermal conductivity, J/(m · s · K)
L = length of constrictor, m
l = mixing length, m
$\dot{m}$ = mass flow rate, kg/s
Pr = Prandtl number
p_c = pressure at the end of the constrictor, atm
$\boldsymbol{Q}$ = conservative variable vector
q_c = conductive heat flux, W/m^2
q_R = radiative heat flux, W/m^2
q_ν = radiative heat flux per unit frequency, W · s/m^2
R = radius of constrictor, m
t = time, s
u = axial velocity, m/s
V = voltage, V
v = radial velocity, m/s
x = streamwise coordinate, m
y = radial coordinate, m
α = angle in the cross-sectional plane from the radial direction to the projected line of sight
$\tilde{\gamma}$ = specific heat ratio
ε = eddy viscosity, m^2/s^2
η = arc heater efficiency
θ = angle between the ray and the outward normal to the cylindrical surface
μ = coefficient of viscosity, kg/(m · s^2)
ρ = density, kg/m^3
σ = electrical conductivity, mho/m
τ = optical thickness
$\tau_{i,j}$ = viscous stress
Ω = solid angle, sr

Subscripts

add = additional dissipation mechanism
energy = turbulence mixing in energy equation
L = endpoint of constrictor
n = nth radiative frequency band
tub = turbulence
w = wall
ν = radiation frequency
0 = starting point of constrictor

Superscript

T = transposition

Introduction

ARC-HEATED wind tunnels are widely used to produce the high-temperature heating environments of reentry flights in a ground-based laboratory. Of the several existing types, the type heated by a segmented constrictor is most widely used. The cost of manufacturing such a device or operating it in an untested environment can be lowered if the operating characteristics can be predicted theoretically. Watson and Pegot[1] were the first to develop a code to calculate the flow in such a device. That code used an optically thin model to describe radiation, had a crude turbulence model, and could not describe the flow behavior accurately in a realistic environment.

Nicolet et al.[2,3] improved the code by introducing a radiation model that accounts for self-absorption and by modifying the turbulence model. The resulting code, ARCFLO, was able to predict

Received 11 August 1999; revision received 16 November 1999; accepted for publication 17 November 1999.

*Graduate Student, Department of Aerospace Engineering. Student Member AIAA.
†Professor, Department of Aerospace Engineering. Senior Member AIAA.
‡Senior Research Scientist, Mail Stop 229-1, Space Technology Division, NASA Ames Research Center. Fellow AIAA.

the operating characteristics of realistic devices with a fair accuracy, provided the conditions in the entrance of the constrictor are given. The entrance condition is needed because ARCFLO, as did the original code developed by Watson and Pegot,[1] solves a parabolic system of governing equations, and solutions are obtained through spatial marching. The ARCFLO code was made openly available by publishing the source code and input data.[2]

The flow in the arc heater is subsonic until it passes the nozzle throat. The upstream pressure is affected by the mass flow rate through the throat. Therefore, when the throat diameter is changed, the upstream pressure changes. In the use of the ARCFLO code, there is no way of knowing the upstream pressure without experimentation. ARCFLO code solves the flow phenomenon only within the constrictor and is oblivious of the phenomena occurring in the upstream and downstream electrode chambers, settling chamber, and the converging section of the nozzle. As a result, the code cannot predict the voltage characteristics correctly and cannot render worthwhile information about the flow at the entrance of the nozzle. Not knowing the conditions at the entrance of the nozzle leads to a great hardship in calculating the flow conditions in the nozzle test section.

In this study, as a way to cure these problems, the modern computational fluid dynamics technique is applied to the problem. The entire flow region starting from the upstream electrode chamber to the nozzle exit is solved using a Navier–Stokes description via a time-marching technique. The problem is, thus, made hyperbolic in time. By doing so, the need to know the upstream flow conditions a priori is eliminated. The flow rate and electrical current are the only required inputs.

It is the intention of the present work to retain as many of the elements in the ARCFLO code as possible, except for the intended conversion from the parabolic to hyperbolic treatment. However, it was found that some elements in the ARCFLO intended to be retained are affected by the conversion. Discretization had to be changed from that in ARCFLO to describe the rapid changes in properties near the wall accurately. The turbulence model had to be changed drastically to be compatible with the existence of the radially inward flow from the constrictor wall, which was neglected in ARCFLO. Specifying the upstream boundary condition in the form of distributed mass flow rate leads intrinsically to numerical instability. Fortuitously this difficulty did not occur because of the strong damping incorporated in the present work.

Chemical equilibrium is assumed in the present work. Thus, the present code, tentatively named Arcflo2, is intended to be used to describe the flow from the upstream electrode to the nozzle throat, which is likely to be nearly in equilibrium. In the region downstream of the throat, the expansion probably causes appreciable thermochemical nonequilibrium, and, therefore, the present solutions are most likely unreliable.

When this code is applied to calculate the experimental conditions given in Ref. 2, it yields values that agree closer to the experimental data than ARCFLO, as will be shown.

Governing Equations

Figure 1 shows the segmented constrictor type arc heater. It consists of an anode chamber, a constrictor, a cathode chamber that acts also as the settling chamber, and a nozzle. An arc spans between the electrodes. The gas in the core, that is, in the path of the arc, is heated directly by the arc by joule heating. Most of the test gas is injected through the constrictor wall with a swirl and is heated by the radiation from the core and by turbulent mixing. Radiation emitted by the core reaches the constrictor wall. The heat absorbed by the constrictor wall is removed by the cooling water circulating through the constrictor disks.

To analyze the flow in this device, the gas is assumed to be in a chemical equilibrium state. The governing equations are the axisymmetric Navier–Stokes equations. In a vector form, they are written as follows:

$$\frac{\partial \boldsymbol{Q}}{\partial t} + \frac{\partial \boldsymbol{E}}{\partial x} + \frac{\partial \boldsymbol{F}}{\partial y} + \boldsymbol{H} = \left(\frac{\partial \boldsymbol{E}_v}{\partial x} + \frac{\partial \boldsymbol{F}_v}{\partial y} \right) + \boldsymbol{H}_v + \boldsymbol{I} \qquad (1)$$

where

$$\boldsymbol{Q} = (\rho, \rho u, \rho v, \rho e_t)^T, \qquad \boldsymbol{E} = (\rho u, \rho u^2 + p, \rho v u, \rho H u)^T$$

$$\boldsymbol{F} = (\rho v, \rho u v, \rho v^2 + p, \rho H v)^T$$

$$\boldsymbol{E}_v = (0, \tau_{xx}, \tau_{xy}, -q_{c,x} - q_{R,x} + u\tau_{xx} + v\tau_{xy})^T$$

$$\boldsymbol{F}_v = (0, \tau_{xy}, \tau_{yy}, -q_{c,y} - q_{R,y} + u\tau_{xy} + v\tau_{yy})^T$$

$$\boldsymbol{H} = (1/y)(\rho v, \rho u v, \rho v^2, \rho H v)^T$$

$$\boldsymbol{H}_v = (1/y)(0, \tau_{xy}, \tau_{yy} - \tau_{\theta\theta}, -q_{c,y} - q_{R,y} + u\tau_{xy} + v\tau_{yy})^T$$

$$\boldsymbol{I} = (0, 0, 0, -j \cdot E)^T$$

where

$$\tau_{xx} = \mu \left(\frac{4}{3}\frac{\partial u}{\partial x} - \frac{2}{3}\frac{\partial v}{\partial y} \right), \qquad \tau_{xy} = \mu \left(\frac{\partial u}{\partial y} + \frac{\partial v}{\partial x} \right)$$

$$\tau_{yy} = \mu \left(\frac{4}{3}\frac{\partial v}{\partial y} - \frac{2}{3}\frac{\partial u}{\partial x} \right), \qquad \tau_{\theta\theta} = -\frac{2}{3}\mu \left(\frac{\partial u}{\partial x} + \frac{\partial v}{\partial y} \right) + \frac{4}{3}\mu \frac{v}{y}$$

The equation of state is

$$p = (\tilde{\gamma} - 1)\rho e = (\tilde{\gamma} - 1)\rho \left[e_t - \tfrac{1}{2}(u^2 + v^2) \right] \qquad (2)$$

The thermodynamic properties, including the specific heat ratio $\tilde{\gamma}$, and the transport properties are calculated by the curve fit formulas given in Refs. 4 and 5.

Radiant Flux Calculation

The radiative transport model in the present code is the same as that in ARCFLO code.[2] As is in ARCFLO, the test gas is assumed to be optically gray. The assumptions used in calculating the radiative heat fluxes are[2] 1) the medium is nonscattering, 2) the constrictor wall is black, 3) the constrictor wall is at a constant temperature, 4) the radiative properties do not vary axially, and 5) the exponential kernel approximation is valid. The radiant flux for frequency v is given as

$$q_v(y) = \int_{\Omega} I_v \cos\theta \, \mathrm{d}\Omega \qquad (3)$$

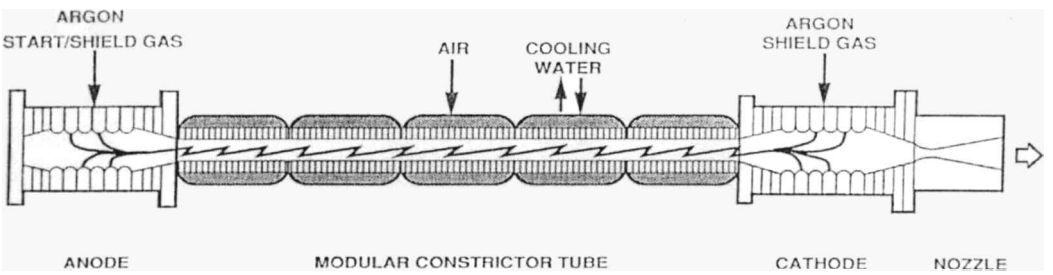

Fig. 1 Schematic of a segmented constrictor type arc-heated wind tunnel.

With assumption 5, the analytic integration over θ is possible, and the radiant flux can be written as

$$q_v(y) = q_v^+(y) - q_v^-(y) \tag{4}$$

where

$$q_v^{\pm}(y) = \int_0^{\pi/2} \cos\alpha G^{\pm}(y, \alpha)\, \mathrm{d}\alpha \tag{5}$$

and the angular directional flux $G^{\pm}(y, \alpha)$ is

$$G^+(y, \alpha) = E_v(R)\exp[-\{\tau(s_1) + \tau(s_2)\}] + \int_0^{\tau(s_1)} E_v(t)\exp[-\{t + \tau(s_2)\}]\,\mathrm{d}t + \int_0^{\tau(s_2)} E_v(t)\exp[-\{-t + \tau(s_2)\}]\,\mathrm{d}t \tag{6}$$

$$G^-(y, \alpha) = E_v(R)\exp[-\{\tau(s_1) - \tau(s_2)\}] + \int_{\tau(s_2)}^{\tau(s_1)} E_v(t)\exp[-\{t - \tau(s_2)\}]\,\mathrm{d}t \tag{7}$$

$$s_1 = \sqrt{R^2 - y^2\sin^2\alpha}, \qquad s_2 = y\cos\alpha$$

The total radiant flux at radius y is calculated as

$$q_R(y) = \int_0^{\infty} q_v(y)\,\mathrm{d}v \tag{8}$$

By the application of the concept of a multiband model, the total radiant flux is written as

$$q_R(y) = \sum_n q_n(y) \tag{9}$$

The two-band model used in the ARCFLO code is adopted in the present work.

A more comprehensive radiation model was used by Sakai et al. to describe radiative transfer in an arc heater.[6] In the model, several thousand bands were considered. Compared with that comprehensive model, the present model tends to underestimate the radiative flux in the hotter central region and to overestimate it in the colder region near the wall because absorption by individual lines in the vacuum-ultraviolet wavelength region is underestimated.

Joule Heating Calculations

By the assumption that the voltage gradient is independent of radius, Ohm's law for a cylindrical column is

$$j(x, y) = \sigma(x, y)E(x) \tag{10}$$

$$E(x) = \frac{j(x, y)}{\sigma(x, y)} = \frac{\int_0^R 2\pi y j(x, y)\,\mathrm{d}y}{\int_0^R 2\pi y\sigma(x, y)\,\mathrm{d}y} = \frac{I}{\int_0^R 2\pi y\sigma(x, y)\,\mathrm{d}y} \tag{11}$$

where

$$I = \int_0^R 2\pi y j(x, y)\,\mathrm{d}y = \text{const}$$

from Kirchhoff's law of conservation of current. Then joule heating is given as

$$j(x, y)\cdot E(x) = \frac{I^2\sigma(x, y)}{\left[\int_0^R 2\pi y\sigma(x, y)\,\mathrm{d}y\right]^2} \tag{12}$$

where the electrical conductivity σ is taken from Ref. 2.

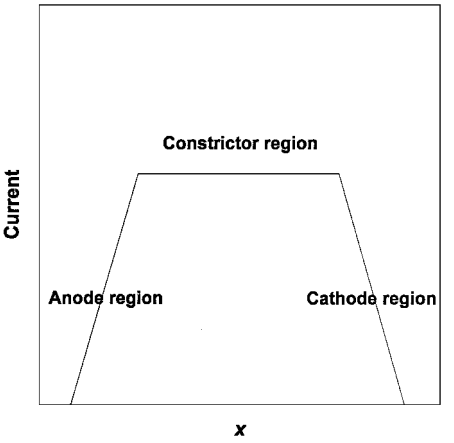

Fig. 2 Schematic of electrical current distribution along axis.

Figure 2 shows schematically the current distribution in the axial direction assumed in the present work. As shown in Fig. 2, current is assumed to increase linearly in the anode chamber, to have a constant value in a constrictor, and to decrease linearly in a cathode region. The linear variation in the electrode chambers implies uniform current density over the electrode surface.

Turbulence Modeling

In this study, the Cebeci–Smith algebraic turbulence model is used as the basis.[7] By this model, the shear stress and the heat flux are written as

$$\tau_{ij} = (\mu + \rho\varepsilon)\frac{\partial u_i}{\partial x_j} \tag{13}$$

$$\dot{q}_i = -\left(\frac{k}{c_p} + \frac{k_{\text{tub}}}{c_{p,\text{tub}}}\right)\frac{\partial h}{\partial x_i} \tag{14}$$

where the eddy viscosity is given by

$$\varepsilon = l^2\left|\frac{\mathrm{d}u}{\mathrm{d}y}\right| \tag{15}$$

$$\frac{k_{\text{tub}}}{c_{p,\text{tub}}} = \rho \times l_{\text{energy}}^2\left|\frac{\mathrm{d}u}{\mathrm{d}y}\right| \tag{16}$$

The mixing lengths l and l_{energy} are defined as follows:

$$l = \sqrt{fac}\times 0.41 \times y \times \left[1 - \exp\left(-\frac{y\sqrt{\rho\tau_w}}{26\cdot\mu}\right)\right] \qquad y_0 \le y < y_c$$

$$l = c \times R, \qquad y_c \le y < R \tag{17}$$

where

$$fac = 0.5 \times \left[0.6 + 50 \times \max\left(10^{-6}, \frac{p_c - 20}{65 - 20}\right)^{0.6}\right]$$

$$c = 0.3 \times (12/p_c)^{0.3}$$

$$l_{\text{energy}} = \sqrt{fac_{\text{energy}}}\times 0.41 \times y \times \left[1 - \exp\left(-\frac{y\sqrt{\rho\tau_w}}{26\cdot\mu}\right)\right] \qquad y_0 \le y < y_c$$

$$l_{\text{energy}} = c_{\text{energy}} \times R, \qquad y_c \le y < R \tag{18}$$

where

$$fac_{\text{energy}} = 0.15 \times \left[0.75 + 5 \times \max\left(10^{-6}, \frac{p_c - 20}{65 - 20} \right)^{0.6} \right]$$

$$c_{\text{energy}} = 0.15 \times \left[1 + 0.5 \frac{(p_c - 15)}{(64 - 15)} \right]$$

and y_0 is a parameter representing the small disturbance from the wall and is obtained from the continuity of l.

Calculation has shown that the original Cebeci–Smith model yields results very different from the experimental data given in Ref. 2. The model predicts a much smaller rate of energy transfer from the core to the surrounding gas volume and, as a result, lower mean enthalpy. This is believed to be because the flow environment in the constricted arc is very different from that of the Cebeci–Smith model. In the constrictor, the flow tends to be strongly turbulent because of the swirling injection of the test gas from the wall. To account for this phenomenon, a mechanism must be postulated that increases energy transfer greatly. Here, an additional viscosity is postulated and added to increase the rate of energy transfer. It was found that, if the additional viscosity is added to the viscous stress, the dissipation near the constrictor wall becomes so large that mass-averaged enthalpy and voltage are calculated inaccurately. Thus, this term is added only to the heat flux in the energy equation. Equation (14) now becomes

$$\dot{q}_i = -\left(\frac{k}{c_p} + \frac{k_{\text{tub}}}{c_{p,\text{tub}}} + \frac{\mu_{\text{add}}}{Pr_{\text{add}}} \right) \frac{\partial h}{\partial x_i} \tag{19}$$

where the Prandtl number for the additional dissipation, Pr_{add}, is taken to be unity. The additional viscosity is given as

$$\mu_{\text{add}} = \mu_{\max} \times x_{\text{dis}} \times y_{\text{dis}} \tag{20}$$

where

$$\mu_{\max} = 9.524 \times 10^{-3} \times i_{\text{dis}} \times \left(\frac{L/D_c}{36.75} \right) \times \left(\frac{\dot{m}}{0.116} \right)^{0.75} \times \left(\frac{0.215}{D_t} \right)^{0.8} \times D_c$$

$$x_{\text{dis}} = \left[\frac{(x - x_0)}{(x_L - x_0)} \right]^{1.5}, \qquad y_{\text{dis}} = \left[\frac{(D_c - y)}{D_c} \right]^{1.5} \tag{21}$$

The value of i_{dis} is defined as follows:

$$i_{\text{dis}} = \{1 - \exp[-(I/c)^b]\} \times (I/500)^{0.5} \tag{22}$$

where $b = 6 - 3[(p_c - 13)/(50 - 13)]$ and $c = 420 - 80[(p_c - 13)/(50 - 13)]$.

There are two additional reasons why the additional eddy viscosity is needed. First, as mentioned in the section "Radiant Flux Calculation," the present radiant model does not describe the phenomenon accurately. In the ARCFLO code, this error is seemingly compensated for by a judicious choice of the turbulence model. The ARCFLO code does not account for the radial inflow of the test gas because it assumes an instant distributed source. In the present Arcflo2 code, which accounts for the radial inflow, the turbulence model used in the ARCFLO code is no longer useful because the radiative transfer phenomenon has a different effect.

The assumption of chemical equilibrium also reduces the radiative heat transfer rate near the constrictor wall. Because radial inflow is not accounted for in ARCFLO, the flow near the wall is calculated in ARCFLO to be hotter than it really is. Thus, ARCFLO needs only a low-energy transfer rate to yield a result that agrees with the experiment. Because the Navier–Stokes method accounts for the radial inflow, the equilibrium temperature in the region near the wall tends to be lower than in ARCFLO. In reality, the electron temperature near the wall will be high because of the low concentration of ions that equalizes electron temperature to the heavy particle temperature and because of the reflection of the electrons by the charged sheath.[8] The high electron temperature will lead to higher radiation absorption and, hence, larger energy transfer. Because this phenomenon is neglected in the present work, the energy transfer to the gas in the vicinity of the wall becomes unrealistically small. Only by artificially increasing the eddy viscosity is this difficulty overcome.

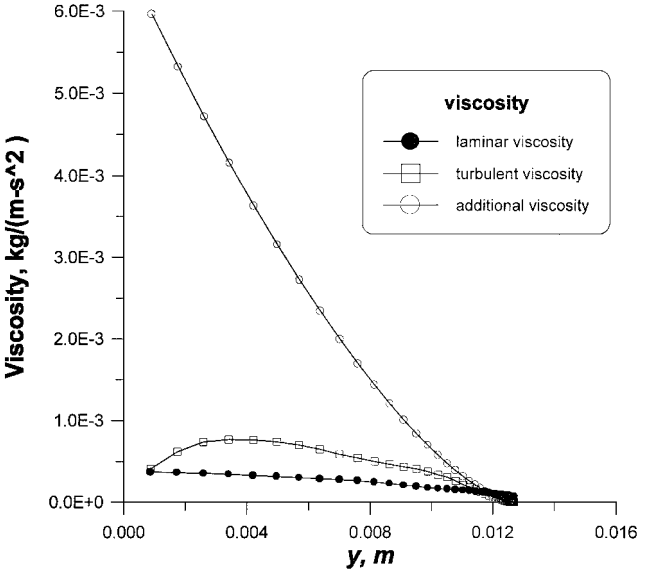

Fig. 3 Radial variation of three components of viscosity for a typical flow environment ($x = 0.9335$ m for case 7).

Figure 3 shows the radial variation of the three components of the viscosity for a typical flow environment. It is apparent that the additional viscosity is dominant over the laminar or the turbulent viscosity of the Cebeci–Smith model. The additional viscosity has a very large value in the core that forces a fast energy transfer from the arc to the surrounding gas.

Boundary Conditions

As mentioned earlier, in an arc heater the test gas is injected mostly from the small holes on the constrictor wall. This phenomenon is modeled in the present work by a uniformly distributed source. The wall is assumed to be at a constant given temperature. The injection velocity is given by

$$V_{\text{injection}} = \dot{m}/\rho_w \cdot 2\pi R \cdot L \tag{23}$$

The outflow condition is specified at a point past the sonic throat. To ensure the flow to be supersonic, the calculation is carried out to a substantially high supersonic location, usually to the nozzle exit. The supersonic outflow boundary condition is implemented by the extrapolation from the inner computational domain.

Time Integration

The problem is formulated explicitly in time. By the use of the approximate factorization–alternate direction implicit (AF–ADI) method, the inviscid term is handled implicitly. The axisymmetric source, joule heating, and radiant flux terms are calculated explicitly. Time stepping is made at a constant time step (3.0×10^{-6} s). Because test gas is injected from the wall, the inflow boundary condition specifies the mass flow rate per unit surface area of the constrictor wall. Ordinarily, this boundary condition tends to produce numerical instability. Such instability does not occur in the present method because of the strong turbulence and additional viscosity. Approximately 20,000 ~ 30,000 time steps were found to be necessary to reduce the root-mean-square error to 10^{-4}. As the mass flow rate through the wall becomes larger, more time is needed for

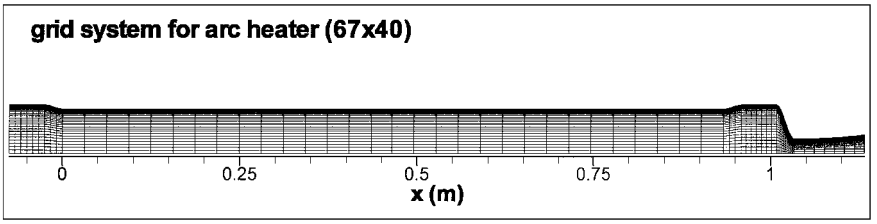

Fig. 4 Typical grid.

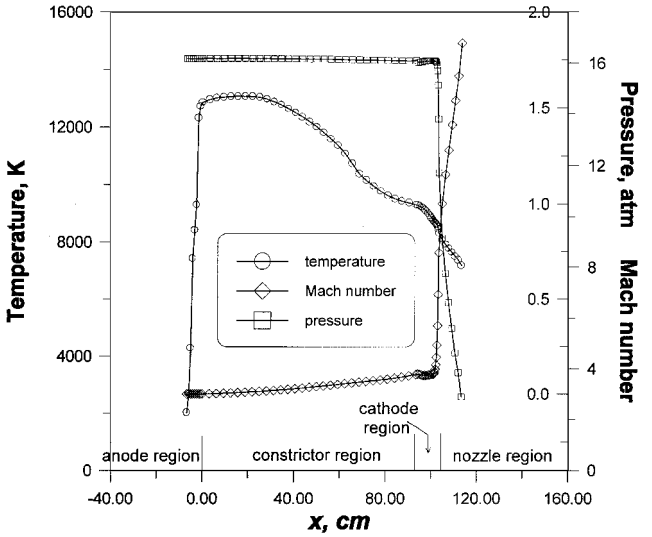

Fig. 5 Distribution of properties along the axis for the sample case.

convergence. With a 67 × 40 grid, the computing time required for convergence was 23,400 s on a 500-MHz DEC Alpha machine.

Results

Here, a typical sample solution is shown in detail. The dimensions of the constrictor are 0.0254-m diameter, 0.9335-m constrictor length, 0.029-kg/s mass flow rate, 1003-A electrical current, 0.00846-m nozzle throat diameter, and 1.648 nozzle area ratio. In Fig. 4, the grid system used is shown magnified by five in the radial direction. The grid dimensions are 67 in the axial direction and 40 in the radial direction. Of the 67 mesh points in the axial direction, 9 points are assigned for the upstream anode chamber, 30 points for the constrictor, 9 points for the cathode chamber (settling chamber), 10 points for the converging section of the nozzle, and 9 points for the diverging section. The grid spacing in the radial direction is 0.0871 cm at the axis and 0.00189 cm at the wall.

In Fig. 5, the flow properties at the centerline are shown along the axis. In Fig. 5, the constrictor spans between $L = 0$ and 93.35 cm. The nozzle throat is at $L = 105$ cm. As expected, Mach number increases linearly within the constrictor. The Mach number at the nozzle exit is 1.825. Temperature decreases from 13,200 K at the upstream end to 9350 K at the exit of constrictor. Within the settling chamber, temperature is initially 9350 K. Temperature becomes 8200 K at the nozzle throat. Pressure is nearly the same from the upstream end to the entrance of the nozzle, $L = 101$ cm. In the nozzle, it falls rapidly, as expected.

Figures 6a–6d show spatial distribution of flow properties. One sees that mass flux increases linearly in the axial direction. Joule heating is confined mostly to the core. The additional viscosity, that is, the viscosity added to the Cebeci–Smith model to bring about agreement with experiment, increases along the constrictor. The radial temperature distribution at $x = L/4$, $L/2$, and L are shown in Fig. 7. Temperature decreases gradually in the radial direction at small radius and decreases rapidly near the wall. As x increases, the centerline temperature decreases, but the wall region becomes hotter. That is, the temperature distribution becomes flatter as x increases.

Figure 8 shows the radial distribution of axial velocity at three different x locations. As expected, the axial velocity varies smoothly in the radial direction. Figure 9 shows the radial distribution of radial velocity at the same x locations. As seen here, radial velocity has a finite negative value at the wall because of the wall injection and is accelerated inwardly initially because density decreases toward the axis because of the increased temperature. As the flow approaches the axis, velocity gradually approaches zero to satisfy the symmetry condition.

In Fig. 10, the radiative heat fluxes in the radially outward direction are shown in the constrictor at three different x locations. Figure 10 shows that radiative heat flux is greater at small x locations. The peak value in the radial variation is especially high at small x locations. Figure 11 shows the joule heating distribution at three different x locations. As x increases, joule heating decreases in the core region but increases near the wall.

Comparison with Experimental Data[2]

To validate the present Arcflo2 code against experimental data, calculations have been carried out for the following two sets of experimental data given in Ref. 2. The calculated voltage, mass-averaged enthalpy, pressure in the constrictor, and the heater efficiency, that is, the ratio of the heat remaining in the flow to the electrical energy supplied, are then compared with the experimental data. Mass-average enthalpy and efficiency are defined as follows.

Mass-averaged enthalpy (J/kg):

$$\bar{h}(x) = \frac{\int_0^R 2\pi y \cdot h(x, y) u(x, y)\, \mathrm{d}y}{\int_0^R 2\pi y \cdot u(x, y)\, \mathrm{d}y} \tag{24}$$

Efficiency (%):

$$\eta = \frac{\text{power absorbed by flow}}{\text{power input}} = 100 \times \left(1 - \frac{q_R - q_c}{I \cdot V_{\text{total}}}\right) \tag{25}$$

Reference 2 provides the geometry of the arc constrictor and nozzle throat diameter but does not provide the geometry of the electrode chambers. The dimensions of the electrode chambers of the arc heater at Arnold Engineering Development Center are assumed to be proportional to those shown in Fig. 1. The dimensions of the electrode chambers for the arc heater in Sandia Laboratory are assumed to be the same as those for the Arnold Engineering Development Center device. The turbulence model in Arcflo2 code described earlier, with the same set of parameters, is used uniformly to all cases. The parameter set related with the turbulent model in ARCFLO code is used as given in Ref. 2.

As seen in Tables 1 and 2, the present Arcflo2 code yields values that agree fairly closely with the experimental data. In the case of high pressures, errors are commonly about 3%, and for low pressures, errors are about 6%.

In Figs. 12 and 13, the radial variation of velocity and temperature is shown for the Sandia Laboratory case. At low currents, the gas is accelerated only in the core region: The velocity in the region near the wall remains small. As current becomes larger, the axial velocity near the wall increases. Beyond certain current values, the velocity and temperature distributions remain unchanged.

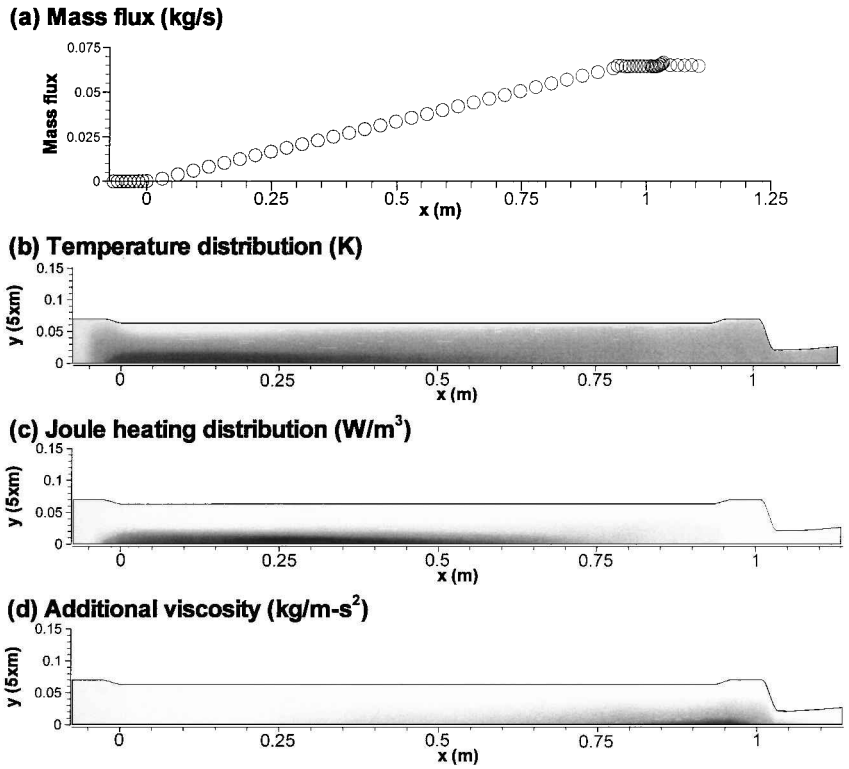

Fig. 6 Spatial distribution of properties for the sample case.

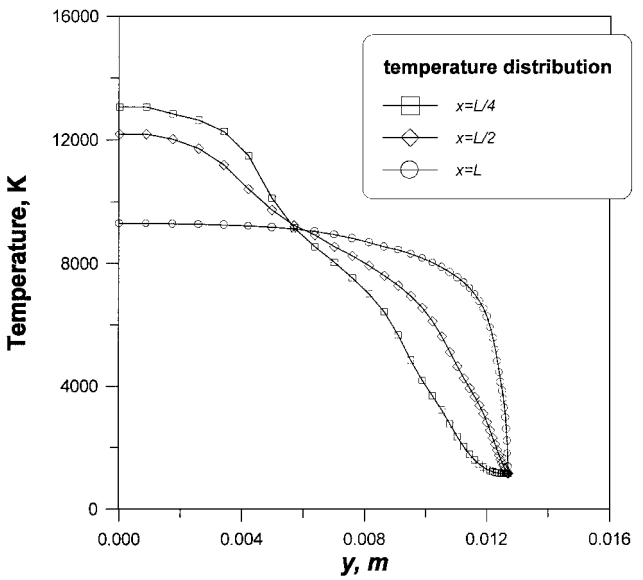

Fig. 7 Radial distribution of temperature in the constrictor at three different x locations for the sample case.

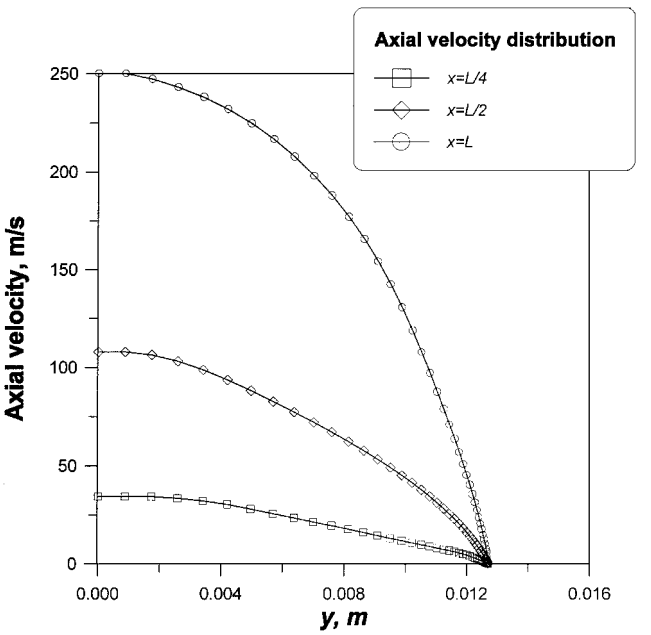

Fig. 8 Axial velocity distribution in the constrictor at three different x locations for the sample case.

In Fig. 14, the measured and calculated mass-averaged enthalpies are compared. The present results generally shows good agreement with the experimental data.

Comparisons of Arcflo2 Code with ARCFLO Code

The Arcflo2 code is compared with ARCFLO code for cases 2 and 11 given in Tables 1 and 2. Case 2 represents a high-pressure operating condition, whereas case 11 is for a high-enthalpy condition. Table 3 shows the comparison of the mass-averaged enthalpy at the downstream end of the constrictor between the two codes. As seen in Table 3, the present code yields values that are closer in agreement with the experimental data than ARCFLO code.

By examination of all solutions, it was found that mass-averaged enthalpy is determined primarily by the ratio of axial distance x to the constrictor diameter D_c and is relatively independent of constrictor diameter, pressure, mass flow rate, or electrical current. The expression

$$\bar{h}(x) = \bar{h}_\infty \times \{1 - \exp[-(x/D_c)/9.75]\}^2 \qquad (26)$$

is proposed to represent the mass-averaged enthalpy values given in Ref. 2. In Fig. 15, this value is shown as curve 1 and is compared with the results of Arcflo2 calculations. As seen here, the approximate

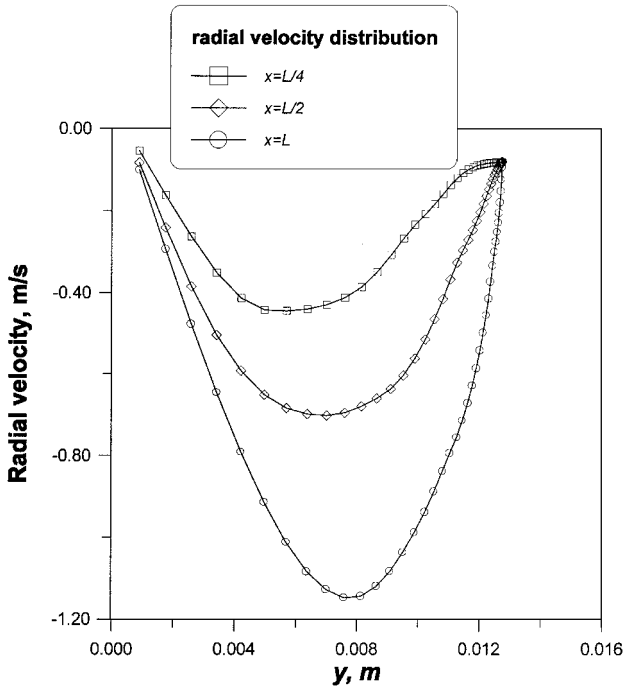

Fig. 9 Radial velocity distribution in the constrictor at three different x locations for the sample case.

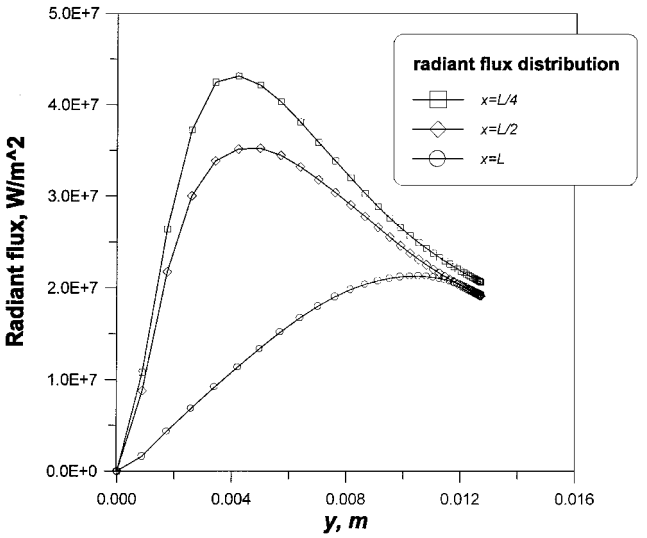

Fig. 10 Radiative fluxes in the radially outward direction in the constrictor at three different x locations for the sample case.

expression agrees with the computed results for x/D_c values above 15.

Table 4 compares the overall voltages calculated by the two methods with the experimental data. Here again, one sees that the present Arcflo2 code agrees better with the experimental data than the ARCFLO code. Figures 16 and 17 compare the mass-averaged enthalpy and voltage distribution for case 11. The experimental values and the values calculated by ARCFLO are indicated also. As seen here, ARCFLO overestimates the voltage and underestimates the mass-averaged enthalpy. For both, the present Arcflo2 code shows better agreement with the experimental data than ARCFLO.

Table 5 shows the comparison of the heater efficiency calculated by the Arcflo2 and ARCFLO codes with the experimental data. As seen in Table 5, ARCFLO predicts greater energy loss than the measured values. The present Arcflo2 code yields efficiency values that are closer in agreement with the experimental data.

Table 1 Comparison of the results of Arcflo2 calculation for Arnold Engineering Development Center data: $D_c = 0.0237$ m, $D_t = 0.00546$ m, and $L = 0.4699$ m

Method	Constrictor voltage, V	Mass-averaged enthalpy, J/kg	Constrictor pressure, atm	Arc-heater efficiency, %
	Case 1, I = *591 A,* $\dot{m}$ = *0.0249 kg/s*			
Exp.	2120	1.626×10^7	26.2	32.4
Arcflo2	2028	1.648×10^7	26.4	31.7
Error, %	4.34	1.37	0.76	2.16
	Case 2, I = *575 A,* $\dot{m}$ = *0.0526 kg/s*			
Exp.	3300	1.387×10^7	53.7	38.5
Arcflo2	3226	1.361×10^7	52.8	37.2
Error, %	2.24	1.90	1.68	3.38
	Case 3, I = *475 A,* $\dot{m}$ = *0.0544 kg/s*			
Exp.	3300	1.239×10^7	53.2	43.0
Arcflo2	3226	1.253×10^7	53.5	39.6
Error, %	2.24	1.15	0.56	7.91
	Case 4, I = *370 A,* $\dot{m}$ = *0.0549 kg/s*			
Exp.	3360	1.067×10^7	51.0	47.1
Arcflo2	3280	1.049×10^7	50.6	45.0
Error, %	2.38	1.66	0.78	4.46
	Case 5, I = *682 A,* $\dot{m}$ = *0.0617 kg/s*			
Exp.	3544	1.369×10^7	64.0	34.9
Arcflo2	3576	1.423×10^7	63.7	36.5
Error, %	0.90	3.98	0.46	4.58
	Case 6, I = *561 A,* $\dot{m}$ = *0.0871 kg/s*			
Exp.	4465	1.226×10^7	84.4	42.6
Arcflo2	4536	1.198×10^7	82.8	41.2
Error, %	1.59	2.28	2.37	3.29

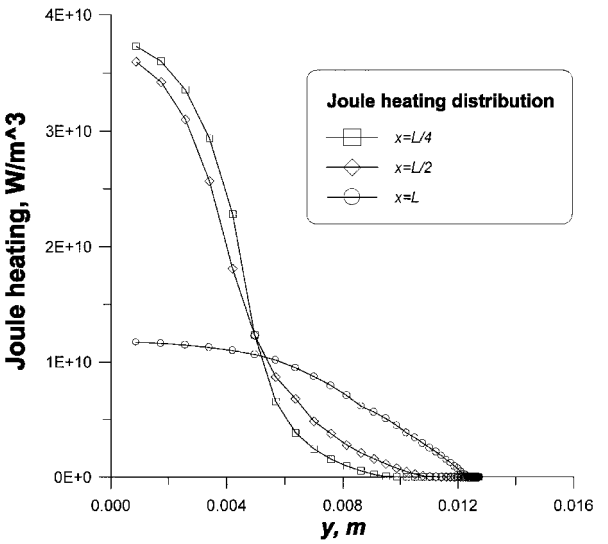

Fig. 11 Joule heating distribution in the constrictor at three different x locations for the sample case.

In Fig. 18, the distributions of temperature and radiative heat flux are compared between the Arcflo2 and ARCFLO codes for case 11. As seen in Fig. 18, ARCFLO seems to overestimate radiative heat transfer compared to the Arcflo2 code. This explains why the ARCFLO code underpredicts efficiency in Table 5.

Discussion

As was intended, the present Arcflo2 code converts the original ARCFLO code into a computational fluid dynamics (CFD) code. As a CFD code, the steady-state solution is obtained as the time-asymptotic solution to a time-dependent problem. As a result, only the mass flow rate and the electrical current are needed as inputs, and no other a priori assumption is needed. The mass injection from the gaps between the adjacent constrictor disks that was not accounted

Table 2 Comparison of the results of Arcflo2 calculation for Sandia Laboratory data: $D_c = 0.0254$ m, $D_t = 0.00846$ m, and $L = 0.9335$ m

Method	Constrictor voltage, V	Mass-averaged enthalpy, J/kg	Constrictor pressure, atm	Arc-heater efficiency, %
		Case 7, I = *352 A,* $\dot{m}$ = *0.0290 kg/s*		
Exp.	2376	1.370×10^7	11.5	47.7
Arcflo2	2270	1.387×10^7	12.1	50.0
Error, %	4.46	1.27	5.22	4.82
		Case 8, I = *413 A,* $\dot{m}$ = *0.0295 kg/s*		
Exp.	2503	1.905×10^7	12.4	54.3
Arcflo2	2581	1.798×10^7	13.5	50.3
Error, %	3.12	5.64	8.87	7.37
		Case 9, I = *551 A,* $\dot{m}$ = *0.0295 kg/s*		
Exp.	2457	2.161×10^7	13.3	47.6
Arcflo2	2608	2.168×10^7	14.4	45.5
Error, %	6.15	0.33	8.27	4.41
		Case 10, I = *778 A,* $\dot{m}$ = *0.0295 kg/s*		
Exp.	2417	2.891×10^7	13.8	45.3
Arcflo2	2613	2.686×10^7	14.6	42.3
Error, %	8.11	7.10	5.80	6.62
		Case 11, I = *1003 A,* $\dot{m}$ = *0.0290 kg/s*		
Exp.	2309	3.019×10^7	14.5	37.8
Arcflo2	2498	3.018×10^7	14.5	37.0
Error, %	8.19	0.02	0.00	2.12

Table 3 Comparison of the results of Arcflo2 calculation with ARCFLO calculation given in Ref. 2 on mass-averaged enthalpy

Case	ARCFLO	Arcflo2	Experiment
2	1.115×10^7	1.361×10^7	1.387×10^7
11	2.491×10^7	3.018×10^7	3.019×10^7

Table 4 Comparison of the voltages among Arcflo2, ARCFLO, and experimental data

Case	ARCFLO, V	Arcflo2, V	Experiment, V
2	2521	3226	3300
11	2542	2498	2309

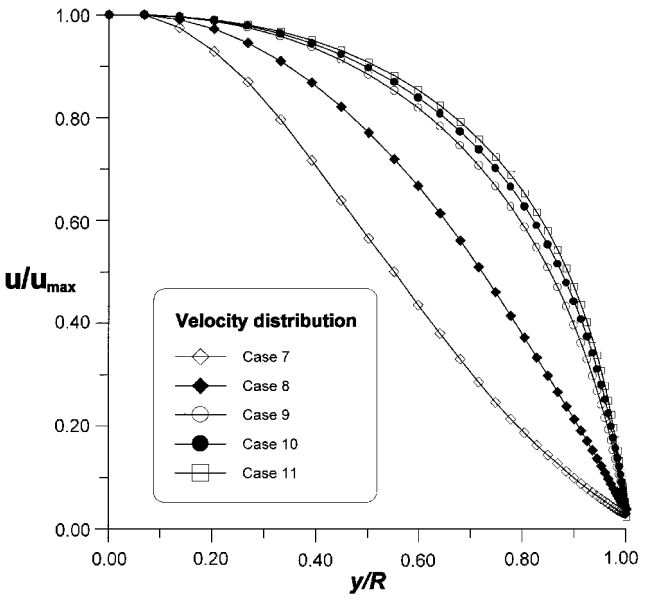

Fig. 12 Radial distributions of axial velocity at the downstream end of the constrictor for Sandia Laboratory data.

Table 5 Comparison of the efficiency values among Arcflo2, ARCFLO, and experimental data

Case	ARCFLO, %	Arcflo2, %	Experiment, %
2	32	37.2	38.5
11	26	37.0	37.8

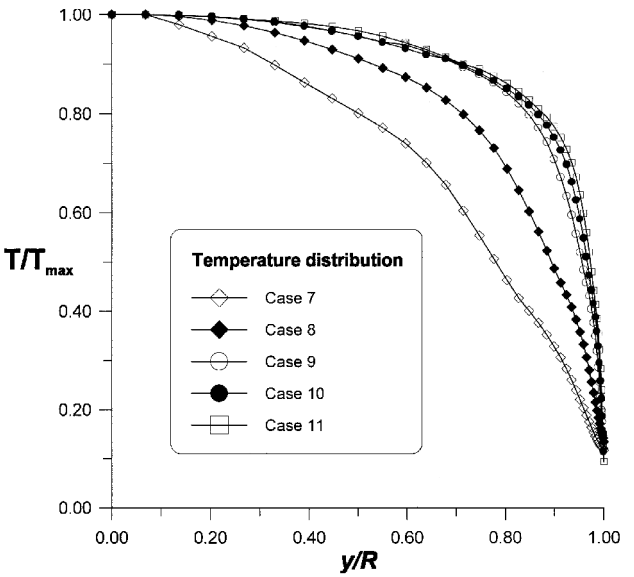

Fig. 13 Radial distributions of temperature at the downstream end of the constrictor for Sandia Laboratory data.

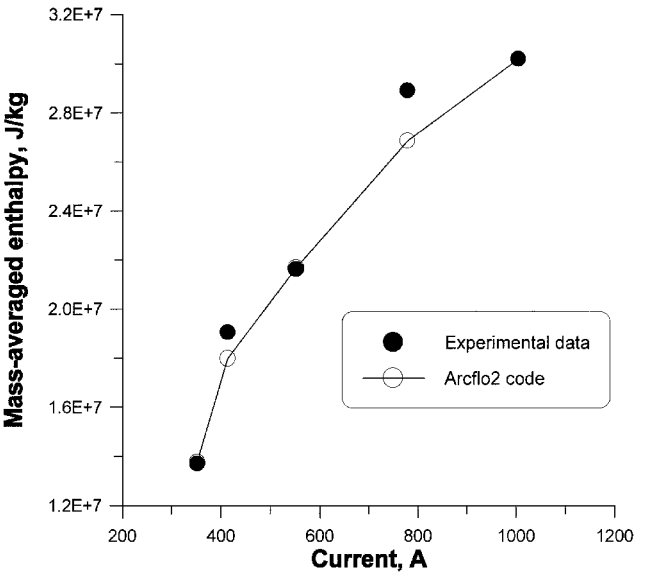

Fig. 14 Comparison of mass-averaged enthalpies between the Arcflo2 calculations and the Sandia Laboratory data.

for in the original ARCFLO is modeled as a source uniformly distributed over the side wall. The consideration of the side-wall injection led to the need for a heat transfer description different from that in ARCFLO. The side-wall injection tends to block the convective heat transfer to the wall. To bring about the same extent of convective heat transfer rates to the wall as in ARCFLO, existence of a strong turbulence had to be assumed. As mentioned earlier, because of the swirl motion, strong turbulence is likely to develop. This turbulence was not accounted for in momentum transfer, because an increased eddy viscosity leads to disagreement with experimental data. This dilemma originates from 1) the inaccuracy in the two-band description of radiative transfer and 2) the assumption

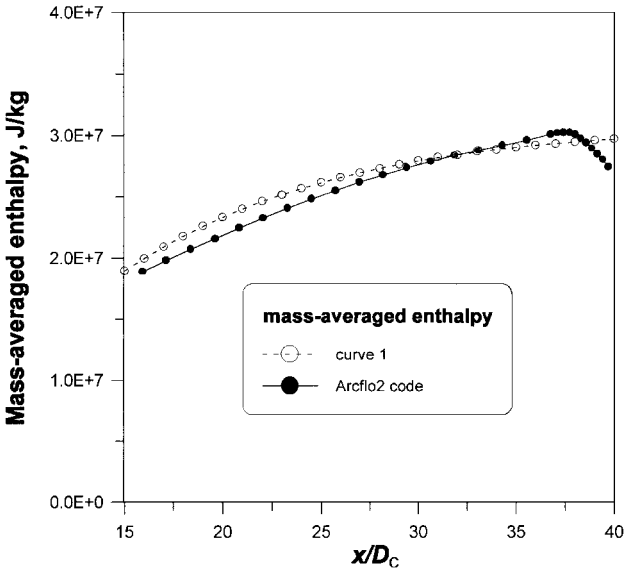

Fig. 15 Curve-fit of mass-averaged enthalpy for case 11.

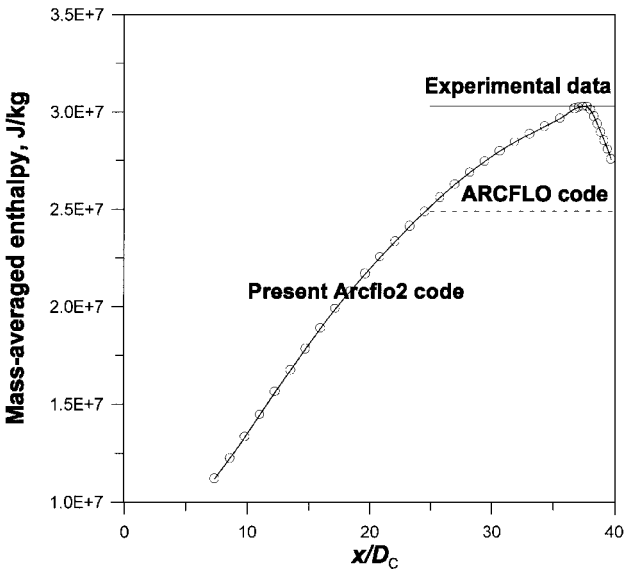

Fig. 16 Comparison of mass-averaged enthalpy distributions calculated by Arcflo2 and ARCFLO codes with the experimental data for case 11.

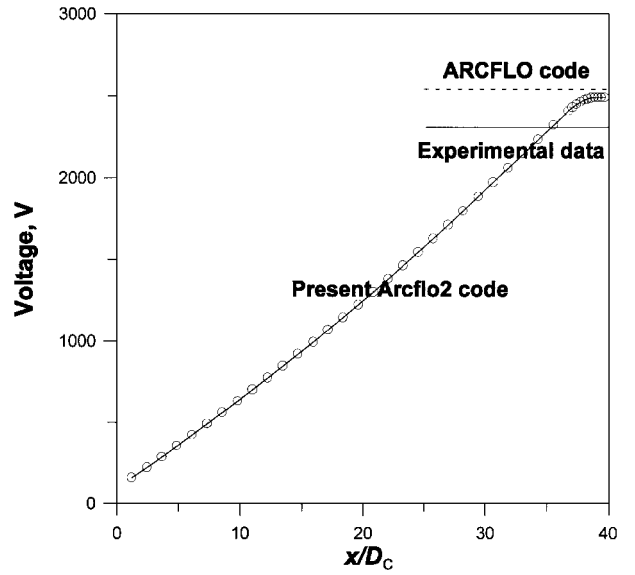

Fig. 17 Comparison of voltage distributions calculated by Arcflo2 and ARCFLO codes with the experimental data for case 11.

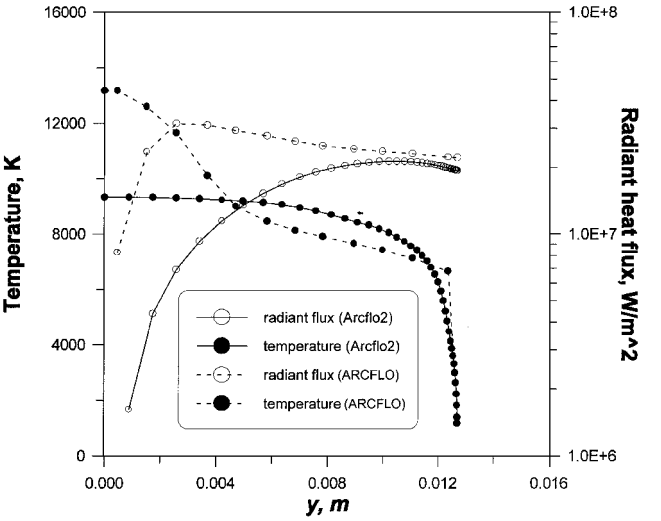

Fig. 18 Comparison of the temperature and radiant flux distributions at the end of the constrictor between Arcflo2 and ARCFLO codes for case 11.

of thermal equilibrium and arises only because the side-wall injection is accounted for. A two-band radiation model used here (and in ARCFLO) is not accurate, as can be seen by comparing with the Planck–Rosseland–Grey gas model.[6] The assumption of thermochemical equilibrium has the following consequences. As mentioned earlier, electron temperature is generally high in the vicinity of the wall, producing a thermal nonequilibrium situation. Because radiative properties are a function mostly of electron temperature, neglecting this phenomenon leads to erroneous energy transfer. In the present code, these shortcomings are offset by introducing the additional viscosity. In the future, an effort should be made to implement a more accurate radiation model and to account for the thermal nonequilibrium phenomenon near the wall.

Conclusions

A Navier–Stokes code, Arcflo2, is developed to compute the flow in a constricted arc-heated wind tunnel. The code needs only the flow rate and electrical current as inputs, and describes the flowfield from the upstream electrode region to beyond the nozzle throat. It adopts the same radiation model as in the ARCFLO code, but has a special turbulence model. The code finds a time-asymptotic solution through implicit time marching. The code yields mass-averaged enthalpy and electrical voltage values that agree better with the existing experimental data than the existing ARCFLO code.

References

[1]Watson, V. R., and Pegot, E. B., "Numerical Calculations for the Characteristics of a Gas Flowing Axially Through a Constricted Arc," NASA TN D-4042, 1966.

[2]Nicolet, W. E., Shepard, C. E., Clark, K. J., Balakrishnan, A., Kesselring, J. P., Suchsland, K. E., and Reese, J. J., "Analytical and Design Study for a High-Pressure, High-Enthalpy Constricted Arc Heater," Arnold Engineering Development Center, AEDC-TR-75-47, Arnold AFB, TN, 1975.

[3]Nicolet, W. E., Shepard, C. E., Clark, K. J., Balakrishnan, A., Kesselring, J. P., Suchsland, K. E., and Reese, J. J., "Methods for the Analysis of High-Pressure, High-Enthalpy Constricted Arc Heaters," AIAA Paper 75-704, 1975.

[4]Srinivasan, S., Tannehill, J. C., and Weilmuenster K. J., "Simplified Curve Fits for the Thermodynamic Properties of Equilibrium Air," NASA RP-1181, Aug. 1987.

[5]Gupta, R. N., Lee, K. P., Thompson, R. A., and Yos, J. M., "Calculations and Curve Fits of Thermodynamic and Transport Properties for Equilibrium Air to 30000 K," NASA RP-1260, 1991.

[6]Sakai, T., Sawada, K., and Mitsuda, M., "Application of Planck–Rosseland–Gray Model for High Enthalpy Arc Heaters," AIAA Paper 98-2838, 1998.

[7]Hirsch, C., *Numerical Computation of Internal and External Flows*, Wiley, New York, 1990, pp. 608, 609.

[8]Park, C., *Nonequilibrium Hypersonic Aerothermodynamics*, Wiley, New York, 1990, p. 140.